Membrane architecture of pulmonary lamellar bodies revealed by post-correlation on-lamella cryo-CLEM

Steffen Klein[1,#], Benedikt H. Wimmer[1,#], Sophie L. Winter[1], Androniki Kolovou[1], Vibor Laketa[2], Petr Chlanda[1,*]

1) Membrane Biology of Viral Infection Group, Center for Integrative Infectious Diseases, University Hospital Heidelberg

2) Infectious Diseases Imaging Platform (IDIP), Center for Integrative Infectious Diseases, University Hospital Heidelberg

# equal contribution

*correspondence to: petr.chlanda@bioquant.uni-heidelberg.de

Abstract

Lamellar bodies (LBs) are surfactant rich organelles in alveolar type 2 cells. LBs disassemble into a lipid-protein network that reduces surface tension and facilitates gas exchange at the air-water interface in the alveolar cavity. Current knowledge of LB architecture is predominantly based on electron microscopy studies using disruptive sample preparation methods. We established a post-correlation on-lamella cryo-correlative light and electron microscopy approach for cryo-FIB milled lung cells to structurally characterize and validate LB identity in their unperturbed state using the well-established ABCA3-eGFP marker. *In situ* cryo-electron tomography revealed that LBs are composed of lipidic structures unique in organelle biology. We report open-ended membrane sheets frequently attached to the limiting membrane of LBs and so far undescribed dome-shaped protein complexes. We propose that LB biogenesis is driven by parallel membrane sheet import and the curvature of the limiting membrane to maximize lipid storage capacity.

Introduction

Pulmonary lamellar bodies (LBs) are specialized organelles exclusively found in alveolar type 2 epithelial cells (AEC2). Their function is to concentrate specialized lipids and proteins that are subsequently released through exocytosis into the alveolar cavity in large amounts. Upon secretion, the LB interior rapidly disassembles into a highly organized network composed of lipids and proteins called pulmonary surfactant. The pulmonary surfactant reduces the surface tension of the air-water interface in the alveoli to facilitate gas exchange during respiration and therefore it must be constantly replenished to sustain breathing function[1].

LBs are composed of a core containing multilamellar concentric membrane sheets surrounded by a limiting membrane as revealed by thin-section transmission electron microscopy (TEM)[2]. LBs contain 85% phospholipids by weight, mostly dipalmitoyl-phosphatidylcholine (DPPC)[3], as well as cholesterol and specialized surfactant proteins A, B and C (SFTPA, B, C)[4]. The majority of the LB associated proteins are commonly found in lysosomes, LBs are thus classified as lysosome-related organelles. Mass spectrometry identified 34 proteins unique to lung LBs[5]. While the core contains the small hydrophobic proteins SFTPB and SFTPC[6], the limiting membrane is enriched in the flippase ATP Binding Cassette Subfamily A Member 3 (ABCA3)[7].

In the current model of LB biogenesis, lipids are flipped by ABCA3 from the cytosolic to the luminal leaflet and are imported into the LB core[8], where SFTPB and SFTPC are responsible for further lipid rearrangement into tightly packed membrane sheets[9]. However, this model has been difficult to validate. The LBs' high lipid content is poorly preserved as a result of room temperature TEM sample preparation, which relies on chemical fixation and dehydration. In consequence, the concentric membranes inside the LB appear wrinkled. Therefore, it is neither understood how they are organized in three-dimensions (3D) nor is it known how the membrane stacks are formed. A study employing cryo-electron microscopy of vitrified sections (CEMOVIS) on rat lungs enabled imaging of frozen-hydrated LBs and showed smooth concentric membranes[10]. However, due to compression artifacts caused by sectioning and lack of compatibility with cryo-electron tomography (cryo-ET)[11], the study provided only little insight into the complex LB architecture.

Unlike CEMOVIS, cryo-focused ion beam (cryo-FIB) milling enables preparation of thin cellular lamellae of arbitrary thickness with a smooth surface and without compression such that they are compatible with cryo-ET[12, 13]. Correlative light and electron microscopy (CLEM) enables unequivocal identification of the targeted compartments and yields structural details[14]. CLEM methods have been adapted to cryo-EM and have successfully been implemented on *in vitro* samples[15, 16] or for cryo-ET performed on whole cells[17-20]. However, a correlation of light microscopy (LM) and electron microscopy (EM) data in a workflow involving cryo-FIB milling is challenging due to the milling geometry and multiple transfers between microscopes: each transfer increases the risk of sample devitrification and ice-contamination. So far, available *in situ* cryo-CLEM workflows involving cryo-FIB milling are aimed at site-specific cryo-FIB milling but do not offer target validation [21].

Here, we propose an alternative strategy and show that precise knowledge of the lamella position in the context of the entire cell determined by LM after cryo-TEM imaging facilitates very accurate mapping of the original LM data to cellular structures on the lamella. In the presented workflow, a 2D correlation is applied to target the region of interest for milling. A second, high precision post-correlation step utilizing LM data acquired after cryo-TEM imaging, deconvolution and 3D correlation is then applied to identify the observed structures.

We applied this novel post-correlation on-lamella cryo-CLEM workflow to study LBs within A549 cells, a model for AEC2[22], that were transiently transfected with ABCA3-eGFP, a well-characterized LB marker[7]. After both correlation steps, 76% of the ABCA3-eGFP signal corresponded to membrane-bound organelles containing either vesicles or lamellated membranes typical for LBs. *In situ* cryo-ET allowed us to structurally characterize the membrane organization in ABCA3-eGFP positive LBs without sample preparation artifacts. The LB core shows tightly packed membrane sheets with uniform spacing and varying curvature. We found parallel bilayer sheets connected to the limiting membrane via three-way lipidic “T”-junctions and concentric bilayer sheets with an open-ended edge as hallmark structures of LBs. In addition, our work revealed a large dome-shaped protein complex on the limiting membrane of some LBs, presumably involved in their formation.

Results

Design of the post-correlation on-lamella cryo-CLEM workflow

We developed a post-correlation on-lamella cryo-CLEM workflow (Fig. 1) which uses cryo-LM imaging after cryo-TEM acquisition to correlate the fluorescence signal with respective cellular architectures captured on the lamella. The workflow does not rely on elaborated targeting algorithms and provides the option to correlate only after assessing the quality of the lamellae by cryo-TEM without introducing ice contamination prior to tilt series (TS) collection. Two cryo-LM maps are acquired, one before cryo-FIB milling and the second after cryo-TEM acquisition. After 3D registration of the two deconvolved cryo-LM maps, a single slice of the registered image stack containing only the fluorescent signal corresponding to the lamella can be extracted and correlated to the cryo-TEM map to identify a structure of interest. As the correlation of cryo-LM and cryo-TEM maps is performed after cryo-ET, we named this approach “post-correlation on-lamella cryo-CLEM”.

To localize LBs in A549 cells, we used ABCA3-eGFP overexpression, which induces the formation of LB-like vesicles[8]. At 48 h post-transfection, A549 cells contained a median of 127 large spherical structures per cell (SD 50, range 45 – 179). The ABCA3-eGFP signal predominantly localized to the limiting membrane and exhibited an average diameter of 1.2 µm (SD 0.8 µm, range 0.1 µm – 4.5 µm) as revealed by confocal microscopy (Supplementary Fig. S1). These measurements are in line with the previously reported LB diameter (range 0.1 – 2.4 µm), based on EM studies performed on lung cells[23].

Transiently transfected A549 cells grown on gold EM-grids were stained with a nucleus dye and a neutral lipid dye to label lipid droplets, which can be used as markers to increase the correlation precision. The neutral lipid dye partially localized to the core of ABCA3-eGFP positive organelles (Supplementary Fig. 2), confirming that ABCA3-eGFP organelles contain lipids. After vitrification by plunge freezing, the sample was transferred under cryogenic temperatures to a cryo-LM to map the EM-grid. Z-stacks in transmitted light bright field (TL-BF) and fluorescent channels were acquired covering a large area (ca. 1.2 mm × 1.2 mm) of the grid to maximize the number of potential areas for subsequent milling. To improve contrast and reduce the signal of stray light of the wide-field microscope setup, as well as to improve the correlation precision, we performed deconvolution of the cryo-LM data (Fig 2). After deconvolution, we were able to discriminate closely apposed ABCA3-eGFP positive organelles, which prior to deconvolution appeared as one organelle (Fig. 2j). Thus, deconvolution improves the lateral and axial resolution of wide-field cryo-LM data.

Maximum intensity projection (MIP) and stitching of cryo-LM data were used to generate a map, from which suitable areas exhibiting large ABCA3-eGFP positive organelles were selected for milling (Fig. 3a). Grids containing 4-6 self-supporting lamellae (Fig. 3b) were transferred to a cryo-TEM where they were mapped to judge overall lamella quality and to localize membrane-bound organelles (Fig. 3c). Among frequently present organelles such as mitochondria and nuclei, membrane-bound structures with a lamellated membrane architecture were selected for cryo-ET as putative LBs. To obtain a fluorescent map of the milled cell for on-lamella post-correlation, grids were mapped a second time by cryo-LM after retrieval from the cryo-TEM (Fig. 3d). Although the lamellae in most cases contained only a partial or no fluorescent signal, likely due to beam-damage, the fluorescent signal in the surrounding body of the cell was preserved. To retrieve the fluorescent signal corresponding to the lamella position we utilized 3D image registration and rigid transformation using one of the deconvolved fluorescence channels to overlay both image volumes (Fig. 3e). The resulting combined image stack incorporates the fluorescent signal before FIB-milling with the TL-BF signal after milling, which contains the precise lamella position. A fluorescent map corresponding to the lamella was extracted from the combined image stack by correcting for the milling angle (Fig. 3f) and finally by extracting the slice corresponding to the plane of the lamella (Fig. 3g). We used the four corners of the lamella as well as clearly identifiable fluorescently labeled markers like lipid droplets and the nuclear envelope as landmarks to correlate the extracted Z-slice with the cryo-TEM map (Fig. 3h) by non-rigid transformation. A detailed view of the correlated cryo-TEM map showed that the ABCA3-eGFP signal overlaps with multi-lamellated structures (Fig. 3i).

Post-correlation on-lamella cryo-CLEM workflow shows a high correlation success rate

To assess the correlation reproducibility of the workflow quantitatively we classified structures corresponding to ABCA3-eGFP isolated signals (n = 62) on 6 lamellae. As a result, 45% of ABCA3-eGFP signal could be assigned to organelles containing lamellated membranes with a displacement smaller than 1 µm. 31% of the ABCA3-eGFP signal was correlated to membrane-bound structures including multivesicular bodies (MVBs), endoplasmic reticulum (ER) or vesicles. The remaining 24% of the ABCA3-eGFP signal could not be assigned to any membrane-bound organelles related to ABCA3 (Fig 3j). Successfully correlated structures showed an average displacement to the local maxima of the corresponding ABCA3-eGPF signal of 450 nm (SD 249 nm). To evaluate the significance of extracting only the signal corresponding to the lamella, we also performed a correlation based on the MIP of the tilt-corrected assembled stack for 3 lamellae. In contrast to extracted slices, 57% of cryo-LM signals could not be assigned to any membrane-bound organelles observed by cryo-TEM when MIP was used for the correlation. Therefore, a correlation using an extracted slice of the fluorescent signal corresponding to the lamella improves the correlation precision by more than 2-fold. In summary, the on-lamella post-correlation approach allowed us to correlate ABCA3-eGFP containing organelles with a 76% correlation success rate and a correlation precision of 450 nm.

LBs contain tightly packed open-ended parallel sheets occasionally attached to the limiting membrane

We analyzed the 3D membrane architecture in tomograms (n = 11) containing ABCA3-eGFP positive organelles (Supplementary Fig. S4). All correlated organelles showed intraluminal vesicles and tightly packed membrane sheets of varying curvature and with regular spacing in the core (Fig. 4a and 4b). In LBs showing large concentric lamellated membrane sheets (Fig. 4e), we observed that the curvature of membrane sheets increases towards the center, concurrent with a spherical 3D organization of the parallel sheets. Detailed analysis of the regular membrane spacing by Fast Fourier transform (FFT) of a central region (Fig. 4j and 4k) revealed three major frequencies which correspond to intra-headgroup-distance (3.7 nm^{-1}), bilayer width (5.5 nm^{-1}) and bilayer repeat (11 nm^{-1}). This is supported by a density line plot of the same area (Fig. 4l). Interestingly, nearly all analyzed organelles (n = 10) showed lamellated membranes with open-ended bilayers rounded with a capping density (Fig. 4c). Some bilayer sheets were connected to the limiting membrane through three-way “T”-junctions as observed in 4 tomograms (Fig. 4h-i). In addition, we observed a crystal-like structure with a lateral repeat of 3.4 nm (Fig. 4e).

Since the architecture of LBs formed by ABCA3-eGFP overexpression might not be representative of the architecture of physiologically formed LBs, we used long-term A549 cultures, which were shown to exhibit a differentiated phenotype with enhanced LB production[24]. We found organelles with a lamellated membrane architecture (Fig. 5e) in 6 out of 21 analyzed tomograms. They exhibited similar morphologies to LBs produced by ABCA3-eGFP overexpression and had an average diameter of 0.58 µm (SD 0.25 µm, range 0.24 – 1.1 µm). Consistent with previously published data[24], we found lamellated structures in only 1 out of 15 analyzed tomograms of short-term non-transfected A549 cells.

Dome-shaped protein complexes localize at the limiting membrane of LBs

After closer inspection of LBs' limiting membranes, we observed a dome-shaped protein complex, hereafter referred to as outer membrane dome protein (OMDP) (Fig. 5a-d). OMDPs appeared hollow and were found in the proximity of ER cisternae partially decorated with ribosomes (Fig. 5b). Although OMDPs were rare (n = 4) in the ABCA3-eGFP transfected A549 cells, they were frequently observed (n = 171) on the limiting membrane of LBs and MVBs in A549 long-term culture from 9 tomograms (Fig. 5e-g). To obtain insights into the OMDP structure, we manually extracted subtomograms (n = 105) containing OMDPs from 2 tomograms and performed subtomogram averaging (STA) in Dynamo[25]. The STA of OMDP revealed a hollow dome-shaped structure (Fig 5h-k) with a base diameter of 30 nm, height of 22 nm with a kink at 7 nm and top diameter of 16 nm. Symmetry search performed on the calculated average indicated that OMDP has a C_8 symmetry. In summary, we identified a novel dome-shaped protein assembly that localizes to the limiting membrane of MVBs and LBs.

Discussion

In this study, we present a workflow for post-correlation on-lamella cryo-CLEM and employ it to study the 3D ultrastructure of LBs under physiological conditions. CLEM approaches are extensively used with chemically fixed or high-pressure frozen-freeze substituted (HPF-FS) samples to identify target structures and rare cellular events[14]. However, such methods are inevitably compromised by sample preparation artifacts from dehydration, post-staining and sample sectioning. In particular, the structure of membranes and lipid-rich organelles is poorly retained due to lipid extraction occurring during sample dehydration by organic solvents. Cryo-EM allows direct visualization of membranous structures close to their native state. Correlative approaches such as cryo-CLEM can be applied to identify molecules within the vitreous sample under the condition that the sample remains vitrified and free of ice contamination during the transfer between cryo-LM and cryo-TEM[15]. Until now, cryo-CLEM workflows involving cryo-FIB milling rely on 3D high-precision correlation for site-specific milling to target the region of interest. A publication by Arnold *et al.*[21] reported lamella preparation with high-precision 3D targeting based on cryo-LM and cryo-FIB/SEM correlation. This workflow was established on suspended cells mixed with fluorescent beads and required a custom-built cryo-stage for a spinning disk confocal microscope. However, in such an approach, the correlation accuracy is highly sensitive to the number and distribution of large fiducial beads that are difficult to control and drift occurring during the milling. In addition, it requires additional instrument time dedicated to correlation before milling[21]. Recently, a prototype microscope with a cryo-LM integrated into the cryo-FIB microscope chamber was developed[26]. This allows monitoring the fluorescent signal during milling and on the finished lamella. This signal can then be directly correlated without a sample transfer. However, in line with our observation, direct detection of the weak signal originating from the < 200 nm thick lamella suitable for cryo-ET is challenging with a wide-field cryo-LM[26].

In this study, we implemented a different strategy and developed a robust on-lamella cryo-CLEM approach taking advantage of high-precision post-correlation suitable for cells cultured directly on EM grids without any beads, utilizing a commercially available Leica cryo-LM. This post-correlation approach permits targeting of transfected cells for cryo-FIB milling without additional instrument time invested for high-precision 3D targeting. Although tilt series

cannot be acquired based on *a priori* acquired fluorescence information, the post-correlation approach gives the opportunity to correlate only vitreous, high-quality lamellae judged by cryo-TEM. In addition, putative organelles of interest can be selected for cryo-ET if their morphology and localization are known from other techniques such as confocal microscopy. Most of our attempts to perform cryo-LM after milling, but prior to cryo-TEM, resulted in increased ice contamination on the lamella, thus preventing high-quality cryo-ET. In addition, we rarely detected fluorescence signal directly on lamellae, which could be due to the sensitivity limits of the Leica wide-field cryo-LM. Thus, a post-correlation on-lamella approach proved to be more effective.

We show that the deconvolution of cryo-LM wide-field data is a necessary step for successful correlation and thus should be applied also to other cryo-CLEM strategies. Computationally performed tilt correction and slice extraction are critical to the workflow even for large organelles like LBs. When applied together, quantification showed that 76% of ABCA3-eGFP signal localized to membrane-bound structures and LB organelles. A residual 24% of signals could not be assigned to any MVB/LB-like structures, likely because of the limited axial resolution of widefield microscopy. Even though deconvolution can improve both lateral and axial resolution, it remains highly anisotropic and much larger than the 150-200 nm lamella thickness. Overexpression of ABCA3-eGFP resulted in fewer LDs compared to naïve A549 cells (Supplementary Fig. 2) and thus in most cases, we were not able to use LDs as correlation markers and the final correlation was performed using the corners of the lamella. Cells containing many LDs such as for example hepatocytes would allow more accurate mapping of the LM data to cellular structures on the lamella using LDs as spatial markers. The correlation precision of the described setup is limited by the aberrations of the microscopes optical system, hence development of cryo-lenses with improved aberration-correction can further improve correlation precision. Furthermore, development of cryo-immersion lenses with a higher numerical aperture (NA)[27] and the implementation of confocal or super-resolution cryo-LM[28] can further improve correlation precision. In addition, integrating cryo-LM imaging into the cryo-FIB/SEM chambers that allows obtaining fluorescence data before and after cryo-FIB milling[26] would be beneficial to avoid sample transfers.

LB ultrastructure has long been subject of debate. Both parallel straight and concentric membrane sheets have been proposed as major structural components of LBs and both types were observed by CEMOVIS[10]. However, cutting artifacts and a lack of 3D data prevented a further understanding of the organelle architecture. Detailed analysis of membrane spacing revealed a repeat of 11 nm, compared to 7.3 nm found by CEMOVIS of rat lungs[10]. This discrepancy could be explained by the compression up to 50% that occurs during sectioning[11].

Post-correlation on-lamella cryo-CLEM combined with *in situ* cryo-ET of ABCA3-eGFP positive organelles allowed us to unravel LB architecture in 3D. The core exhibits multiple concentric bilayers with increasing curvature towards the center. However, none of the LBs observed were exactly centrosymmetric, which had previously been proposed based on polarized light microscopy[29]. “T”-junctions can be observed on the inner leaflet of the limiting membrane, where membranes are pushed into the lipidic core as parallel sheets consistent with a model proposed by Pérez-Gil[9].

Our finding that 40% of the assigned ABCA3-eGFP signal localizes to membrane-bound organelles like MVBs, ER or vesicles is concurrent with previous data on trafficking and proteolytic processing of ABCA3 in LAMP3 positive vesicles[30]. The A549 long-term culture

showed an increased number of organelles compared to short-term non-transfected cells. These organelles were morphologically similar to those induced by ABCA3-eGFP overexpression, indicating that lamellar organization of the ABCA3-eGFP positive organelles are not artifacts of overexpression. Since no LB marker was used to localize LBs in A549 long-term culture, we performed cryo-ET on both cryo-FIB-milled cells and the periphery of whole cells. Interestingly, the majority of large LBs was found in the cell periphery of A549 long-term culture, where LB maturation and surfactant secretion occur.

We identified a dome-shaped protein complex on the LB outer membrane that to our knowledge has not been reported yet. STA revealed that OMDPs exhibit a hollow cage-like structure, however, the limited number of the averaged OMDPs prevented to obtain molecular details of the complex. Nevertheless, based on the indicated C_8 symmetry we speculate that the complex is built of multiple subunits composed of protein assemblies symmetrically organized around a single rotation axis. Notably, we frequently observed the structurally well-characterized 13 MDa major vault protein (MVP) in the cytosol of A549 cells, which forms large cage structures with 39-fold dihedral symmetry[31]. However, the dimensions of the terminal caps of the MVP are different from the OMDP, indicating that OMDP is not derived from MVP (Supplementary Fig. 3). OMDPs were usually observed in close proximity to ER cisternae. It is thus tempting to hypothesize that the complex could be involved in the maintenance of organelle-contact sites. It has long been speculated that a distinct transport mechanism for newly synthesized phospholipids from the ER to LBs must exist[32]. Therefore, consistent with its localization, OMDP could be implicated in this transport. Although OMDP was rarely detected in ABCA3-eGFP expressing cells, it was frequently observed in A549 long-term culture. We believe that the low occurrence of OMDP in ABAC3-eGFP overexpressing A549 cells can be explained by high ABCA3 occupancy on the limiting membrane, causing a displacement of other proteins. Since OMDP has been also observed on MVBs, we assume that this complex plays a more general role in endo-lysosomal trafficking.

Based on structural analysis of ABCA3-positive organelles as well as LBs found in the A549 long-term culture, we propose a model for LB biogenesis (Figure 6): ABCA3-mediated membrane lipid asymmetry causes the inner leaflet to push bilayers into the lumen forming “T”-junctions. It is conceivable that ABCA3 itself or other proteins are responsible for the concentration of phospholipids into membrane sheets. SFTPB contains amphipathic helices[6] that might be responsible for capping the open edges of the membrane sheets. These sheets are cleaved and shaped according to the principal spherical curvature of the LB to maximize the lipid storage capacity per given volume. Finally, OMDP observed on the limiting membrane might regulate LB trafficking and maintain lipid influx through LB-ER contact sites.

In conclusion, we developed and implemented a robust post-correlation on-lamella cryo-CLEM workflow. This workflow can be applied to prove organelle identity using any fluorescent marker to reveal the structural details of organelles in the context of the native cellular environment.

Methods

Cell lines and cell culture

A549 cells[22] were purchased from ECACC (Lot 16J012) and cultured in DMEM/F12 medium (ThermoFisher Scientific) supplemented with 10% (v/v) fetal bovine serum (FBS) (ThermoFisher Scientific) and 100 U/ml Penicillin-Streptomycin (ThermoFisher Scientific) at 37°C, 5% CO_2. A549 long-term culture was maintained without subculturing according to a protocol by Cooper *et al.* [24] in Ham's F12 (Sigma-Aldrich) supplemented with 10% FBS and 100 u/ml Penicillin-Streptomycin (ThermoFisher Scientific) for 28 days. The medium was exchanged twice a week. To prepare samples for plunge-freezing, 200 mesh Quantifoil™ Au R2/2 grids were plasma-cleaned in a Gatan Solarus 950 for 10 sec, sterilized by dipping into 70% Ethanol, placed in a 35 mm dish (ThermoFischer Scientific) coated with a thin layer of polydimethyl siloxane (PDMS, Dow Europe GmbH) and incubated in 1 ml of medium at 37°C for 30 min. Subsequently, the medium was removed and 1.2×10^5 cells were seeded on grids placed in the PDMS-coated dish containing 2 ml of medium. The next day, cells were transiently transfected with 3 µg hABCA3-eGFP plasmid in Mirus™ Trans-IT LT1 transfection reagent. 48 h post transfection the medium was removed, and the cells were incubated in fresh medium containing 1 µg/ml Hoechst 33342 (Sigma-Aldrich) and 150 nM LipiBlue (Dojindo Europe) to stain nucleus and lipid droplets, respectively. After 30 min incubation, cells were washed three times with medium.

Vitrification

Cells were plunge-frozen into liquid ethane immediately after fiducial staining (correlation) or 48 h after seeding (long-term culture) using a Leica EM GP2 automatic plunge-freezer. Cryogen temperature was set to -185°C and the chamber to 25°C and 95% humidity. Grids were blotted from the back with Whatman® Type 1 paper for 4-5 sec. 5 µl medium was added to the grid just before plunge-freezing. For samples that were used for whole-cell tomography, Protein-A Gold fiducials with a nominal diameter of 10 nm (Aurion) were added. Grids were inserted into AutoGrids™ (ThermoFisher Scientific) designed for FIB milling.

Cryo-fluorescence widefield microscopy

Fluorescent maps of vitreous samples were acquired using a Leica EM Cryo-CLEM widefield microscope equipped with a 50× air objective (NA 0.9), Metal Halide light source (EL6000), an air-cooled detector (DFC9000GT) and a cryo-stage cooled to -190°C. A square of approximately 1.2 mm by 1.2 mm was acquired in the center of the grid using the LAS X Navigator. For each field of view, a symmetrical 30 µm Z-stack with a 300 nm spacing was acquired around the autofocus point. The following channels were used: TL-BF, DAPI (Ex: BP 350/50, Em: 460/50) and GFP (Ex: BP470/50, Em: 525/50). TIF files were exported from LAS X and a maximum-intensity projected map was stitched using the Grid/Collection stitching plugin[33] in ImageJ/FIJI[34].

Deconvolution of cryo-fluorescence widefield microscopy data

To increase the clarity of the fluorescence signal, image stacks containing cells of interest were subjected to deconvolution in AutoQuant X3 (Media Cybernetics). A theoretical point-spread function (PSF) was utilized based on microscope and lens specifications (NA 0.9, 50× lens, refraction index 1) and refined over 100 iterations.

Cryo-FIB-SEM milling

After cryo-fluorescence imaging, self-supporting lamellae were prepared using cryo-FIB milling on an Aquilos dual-beam FIB-SEM microscope (ThermoFisher Scientific) as first described by Rigort *et al.*[12]. Transfected cells were selected using correlation with a stitched MIP fluorescence map obtained in the previous step using the MAPS 3.3 software (ThermoFisher Scientific). Cells were coated with an organo-metallic platinum layer for 5-6 sec and gradually thinned in 4 steps at a stage angle of 15-18° using a Ga^+ beam to yield lamellae with 150-200 nm thickness after the final milling step. If possible, micro-expansion joints were used as described by Wolff *et al.*[35] to improve lamella stability. Progress was monitored by SEM imaging at 2.2-10 kV with ETD and T2 detectors.

Tilt series acquisition and tomogram reconstruction

After lamella preparation, grids were transferred to a Titan Krios cryo-TEM operated at 300kV (ThermoFisher Scientific) equipped with a K3 direct electron detector and a Gatan imaging filter (Gatan). Image acquisition was controlled using SerialEM[36]. First, low-magnification maps (LMM) were acquired at 135× magnification to find the lamellae, then medium-magnification maps (MMM) were acquired at 8,700× for correlation and the identification of sites for tilt series (TS) acquisition at 26,000× or 33,000× (corresponding pixel sizes at the specimen level: 3.356 and 2.671 Å, respectively). TS were acquired using a dose-symmetric scheme[37] with a constant electron dose of approx. 3 $e^-/Å^2$ per projection, target defocus -5 μm, energy filter slit at 20 eV, covering the range from 60° to -60° in 3° increments. On-lamella tomography was done with a stage tilted to 6° to compensate for the pre-tilt of the lamella with respect to the grid. Each projection was acquired in counting mode using dose fractionation and 20-40 individual frames, which were aligned and summed using SEMCCD plugin in SerialEM. Whole-cell tomography was performed as stated above with the exception that the TS were acquired at magnification 33,000× (pixel size at the specimen level: 4.302 Å) using a K2 direct electron detector instead of K3 direct electron detector.

TS were processed using the IMOD package[38]. TS were aligned using patch-tracking. Before reconstruction, the contrast transfer function (CTF) was corrected by phase-flipping and the micrographs were dose-filtered. Tomograms were reconstructed using the weighted back-projection algorithm with a SIRT-like filter equivalent to 10 iterations. For power spectral analysis in Fig. 4, tomograms were reconstructed using the SIRT algorithm implemented in 3dmod.

3D rendering of reconstructed tomograms

Renderings were created in Amira 2019.3. First, a subvolume was extracted and manually segmented based on image enhancement and thresholding. Based on this, a convoluted neural network was trained using the interface implemented in Amira 2019.3. The output was used to visualize membranes in the full tomogram.

Subtomogram averaging

STA was performed in Dynamo[25]. Particles (n=105) were picked manually in 2 tomograms and 100 voxel subtomograms were extracted using a crop-on-wall function with the initial particle orientation assigned normal to the segmented limiting membrane of the LB. An initial reference was generated by averaging all 105 particles and the average was iteratively refined using a half-dome shaped mask. A symmetry scan was performed using a focused mask on the top of the cage assembly. Subsequently, the average was further refined using the C_8 symmetry.

Post-correlation on-lamella correlation workflow

After the vitrification of fluorescently labeled cells by plunge freezing, grids were mapped on the Leica cryo-LM. The grid was transferred to a dual-beam cryo-FIB/SEM. By low-precision correlation of the maximum intensity projected (MIP) fluorescent map with the SEM map of the grid, cells of interest were selected and FIB-milled. After a second transfer of the sample to the 300 kV cryo-TEM, the lamellae were mapped, areas of interest were selected, and tilt series were acquired. To facilitate high precision post-correlation of the lamellae, the grids were recovered after the cryo-ET acquisition and the lamellae were mapped a second time in the cryo-LM to reveal the exact lamella positions on the grid. To merge the fluorescent signal from the first cryo-LM map with the information of the lamella position on the second cryo-LM map, the deconvolved stacks were registered in MATLAB 2018b using the *imregtform* function with a custom script (see code availability). A rigid transformation matrix including translation and rotation was calculated based on the same fluorescent channel of both cryo-LM maps respectively. The remaining channels including TL-BF from the second cryo-LM map were transformed by applying the calculated transformation matrix. The fluorescent channels of the first cryo-LM map were merged with the transformed TL-BF channel of the second cryo-LM in FIJI/ImageJ and saved as a composite TIF. To compensate for the FIB-milling angle, the composite stack was resliced using FIJI/ImageJ. Using the TL-BF channel, the actual lamella tilt in the stack was measured, and the composite stack was rotated accordingly to compensate for the tilt. The Z-slice of the lamella was identified and extracted after a second reslice in FIJI/ImageJ. This single tilt-corrected slice was correlated with the stitched TEM-map using a non-rigid 2D transformation in ec-CLEM[39] utilizing the four corners of the lamella as well as clearly identifiable fluorescently labeled organelles like lipid droplets as landmarks.

Correlation precision analysis

To evaluate the success rate and precision of the post-correlation on-lamella cryo-CLEM workflow, the final correlation of the MMM and cryo-LM map was analyzed for 6 lamellae. Local maxima of the cryo-LM map were calculated using FIJI/ImageJ using a tolerance threshold of 10. For each local maximum, ultrastructures of the correlated MMM in a spherical area (radius = 1 µm) were classified either as LB or membrane-bound organelle (MVBs, ER, vesicle). Mitochondrial or nuclear membranes as well as areas without any membrane-bound structures were classified as unspecific. For each assigned ultrastructure, the distance and angle to the center of the local maximum was measured and plotted as a radar plot to estimate the correlation precision.

Confocal fluorescence microscopy

Confocal microscopy of A549 cells transfected with ABCA3-eGFP was done using a Leica SP8 TCS laser scanning confocal microscope equipped with a 63× 1.4NA oil immersion objective and an environmental control chamber heated to 37°C. Image analysis was performed in ImageJ/FIJI[34]. Automated 3D segmentation of ABCA3-eGFP structures was done in Imaris 9.5.1 (Bitplane) after deconvolution in AutoQuant X3.1 (Media Cybernetics).

Code availability

The FIJI/ImageJ macro for fluorescent map assembly and the MATLAB code used for 3D stack registration are available on github under https://github.com/steffen-klein

Acknowledgments

We would like to thank Dr. Surafel Mulugeta for kindly providing the plasmid hABCA3-eGFP. We thank Dr. Stefan Pfeffer for critical reading of the manuscript. We would like to acknowledge microscopy support from the Infectious Diseases Imaging Platform (IDIP) at the Center for Integrative Infectious Disease Research Heidelberg. We would like to acknowledge access to the infrastructure and support provided by the Cryo-EM Network at the Heidelberg University (HD-cryoNet). This work was supported by the Deutsche Forschungsgemeinschaft (Project 19, SFB1129).

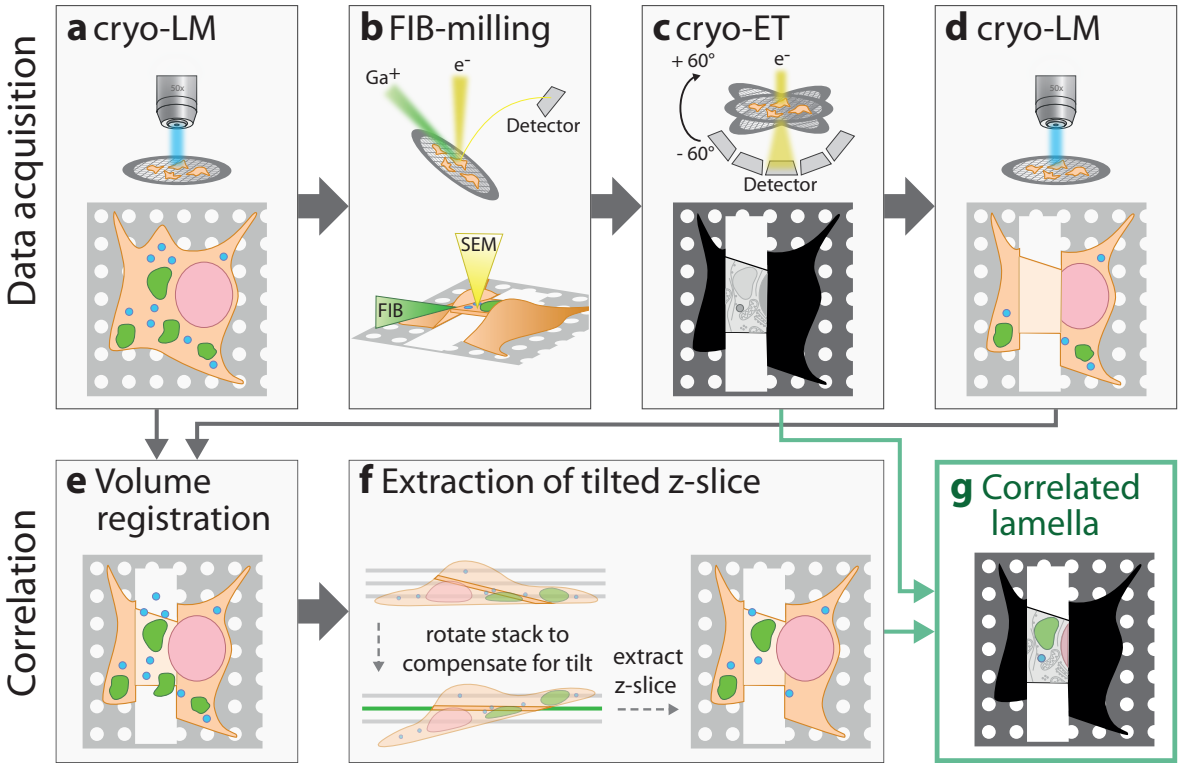

Fig. 1 | Schematic workflow for post-correlation on-lamella cryo-CLEM. The workflow consists of two parts: data acquisition (**a-d**) and data processing for correlation analysis (**e-g**). Structures in cells grown on EM-grids are fluorescently labeled prior to vitrification by plunge-freezing. **a**, In the first step, the vitrified sample is mapped by cryo-LM, acquiring Z-stacks with a 300 nm spacing. **b**, In the second step, labeled cells are thinned by cryo-FIB-milling to produce lamellae of 150 - 200 nm thickness. **c**, Lamellae are mapped by cryo-TEM and tilt series of areas of interest are acquired. **d**, FIB-milled areas are mapped again by cryo-LM to retrieve the exact position of the lamellae. For both Z-stacks of step (**a**) and step (**d**), deconvolution is performed to increase the resolution (not shown in the figure). **e**, To combine the information of the fluorescent signal from step (**a**) and the lamella position from step (**d**), both Z-stacks are aligned using an automated 3D registration algorithm. After image registration, the TL-BF channel of step (**d**) is combined with the fluorescent channels of step (**a**) leading to a combination of lamella position and fluorescent signal in a single composite Z-stack. **f**, To compensate for lamella tilt, the tilt is measured using the TL-BF signal, the Z-stack is rotated accordingly and a Z-slice corresponding to the lamella is extracted. **g**, Finally, the extracted Z-slice is registered to the cryo-TEM map from step (**c**).

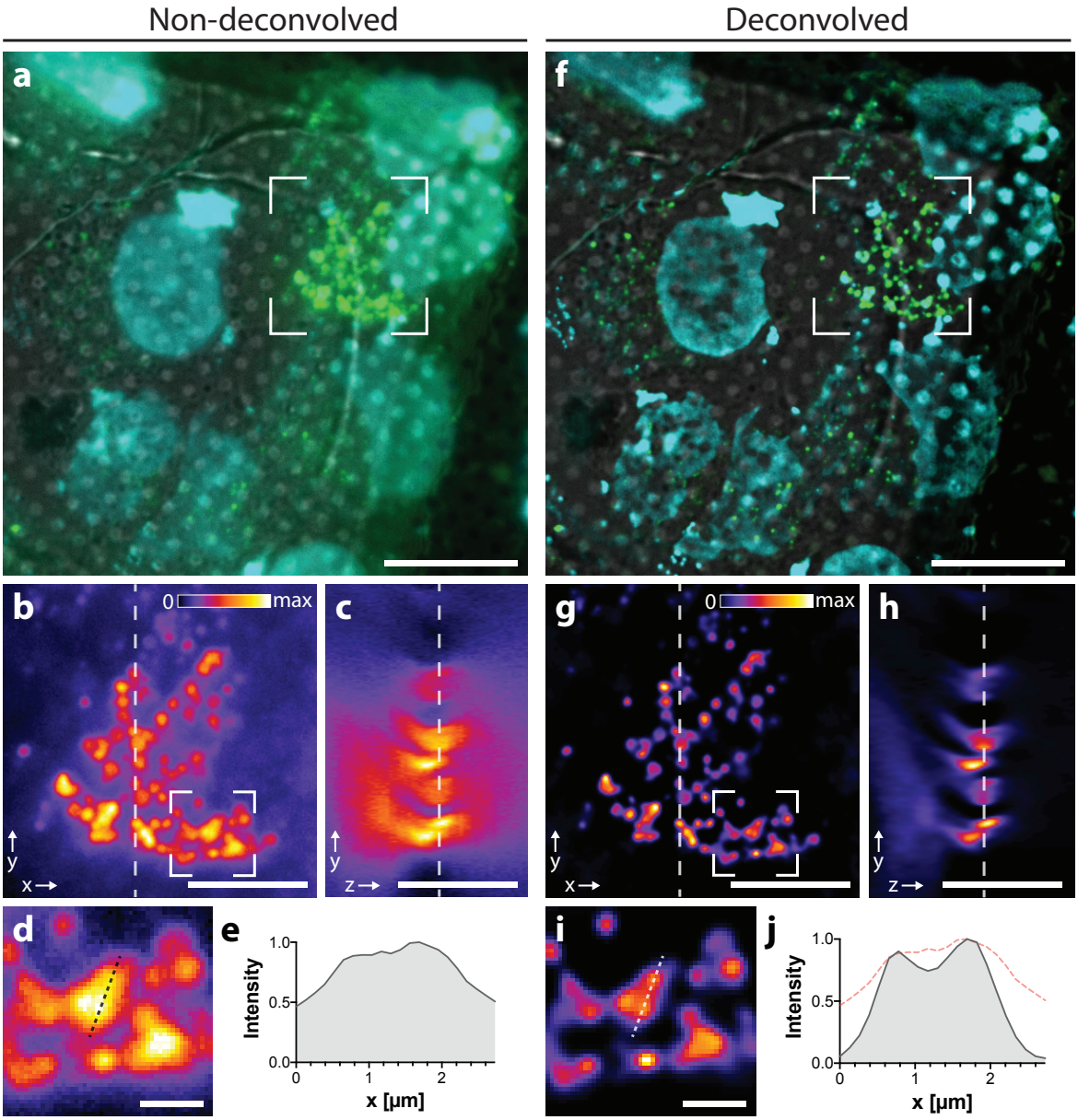

Fig. 2 | Deconvolution improves resolution of cryo-LM wide-field fluorescent images. A549 cells were grown on EM-grids and transfected with ABCA3-eGFP. Nuclei and lipid droplets were fluorescently labelled. After vitrification, the EM-grid was mapped by cryo-LM, acquiring 30 µm thick Z-stacks with a spacing of 300 nm. (**a-e**) show the data before deconvolution, and (**f-j**) after deconvolution. **a** and **f,** Single XY-slice of the acquired Z-stack with the TL-BF channel in grayscale, ABCA3-eGFP in green and the combined signal of the lipid droplet and nucleus stain in cyan. The images show the full dynamic range of the data. **b** and **g**, Details of the same area showing only the ABCA3-eGFP signal, while **c** and **h** show a single ZY plane. Respective plane positions are indicated by dashed lines. **d** and **i**, For further analysis, areas indicated in **(b)** and **(g)**, are enlarged and intensity was measured along the indicated lines. **e**, Line profile of adjacent LBs before deconvolution. **j**, Line profile showing separation of signals after deconvolution (gray). Profile before deconvolution is given as comparison (dashed red line). Scale bars: **(a and f)** 20 µm, **(b, c, g, h)** 10 µm, **(d & i)** 2 µm.

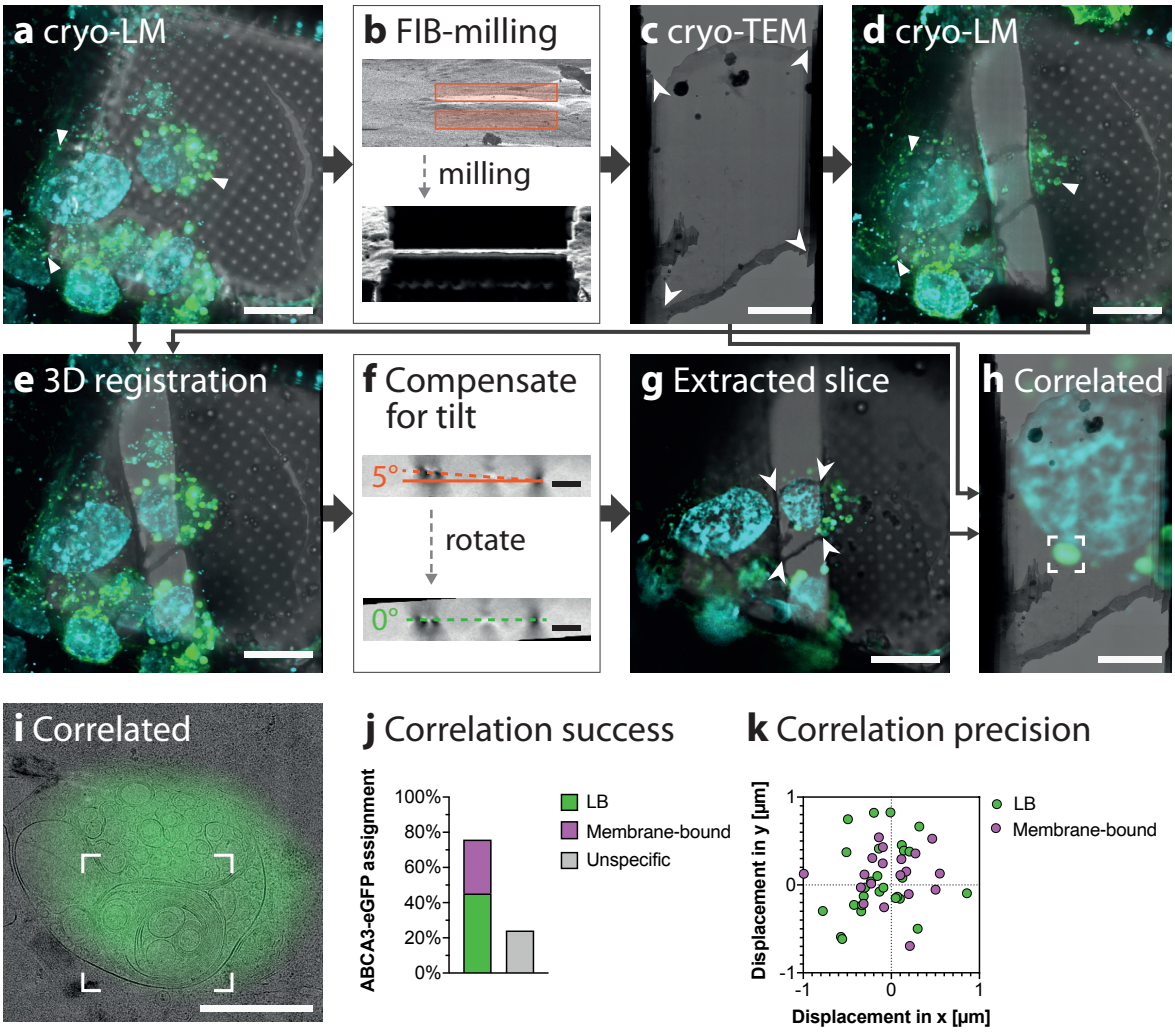

Fig. 3 | Post-correlation on-lamella cryo-CLEM allows the identification of LB-like structures. A549 cells grown on EM-grids were transiently transfected with ABCA3-eGFP, nuclei and lipid droplets were fluorescently labelled prior to plunge freezing. **a,** MIP of the deconvolved cryo-LM stack acquired before FIB-milling. ABCA3-eGFP is shown in green, and nuclei and lipid droplets are shown in cyan. **b,** Angled FIB image showing the same region before and after milling, respectively. **c,** Stitched cryo-TEM map of the lamella produced by FIB milling acquired at 8,700× magnification. White arrowheads show landmarks used for correlation. **d,** MIP of the deconvolved cryo-LM stack acquired after TEM imaging. Fluorescent signal in the cell body remains visible (arrows). **e**, MIP of the registered and aligned image stack. **f,** ZY-slice showing the lamella tilt corresponding to the FIB milling angle (top) and ZY-slice after rotation of the Z-stack. **g,** Extracted Z-slice corresponding to the plane of the lamella. White arrowheads indicate landmarks overlaid with those in **(c). h,** Overlay showing the product of the non-rigid alignment between the TEM map in panel **(c)** and the fluorescence image in panel **(g)**. **i,** High magnification image of the correlated lamella. Location of the tilt series shown in Fig. 4 is highlighted. **j,** Quantification of correlation success rate. A total of n = 62 distinct correlated eGFP signals of 6 lamellae (Supplementary Fig. S4) were assigned to corresponding structures of the cryo-TEM map. 28 ABCA3-eGFP signals were assigned to LDs, 19 to membrane-bound organelles and 15 could not be assigned to any structure. This results in an overall success rate of 76% **k**, Quantification of the correlation precision. For the n = 47 successfully correlated structures, the distance and angle to the center of the corresponding ABCA3-eGFP

signal was measured and plotted as radar plot. The average correlation precision is 450 nm (SD 249 nm). Scale bars: **(a, d, e, g)** 20 µm, **(c, f, h)** 5 µm, **(i)** 1 µm

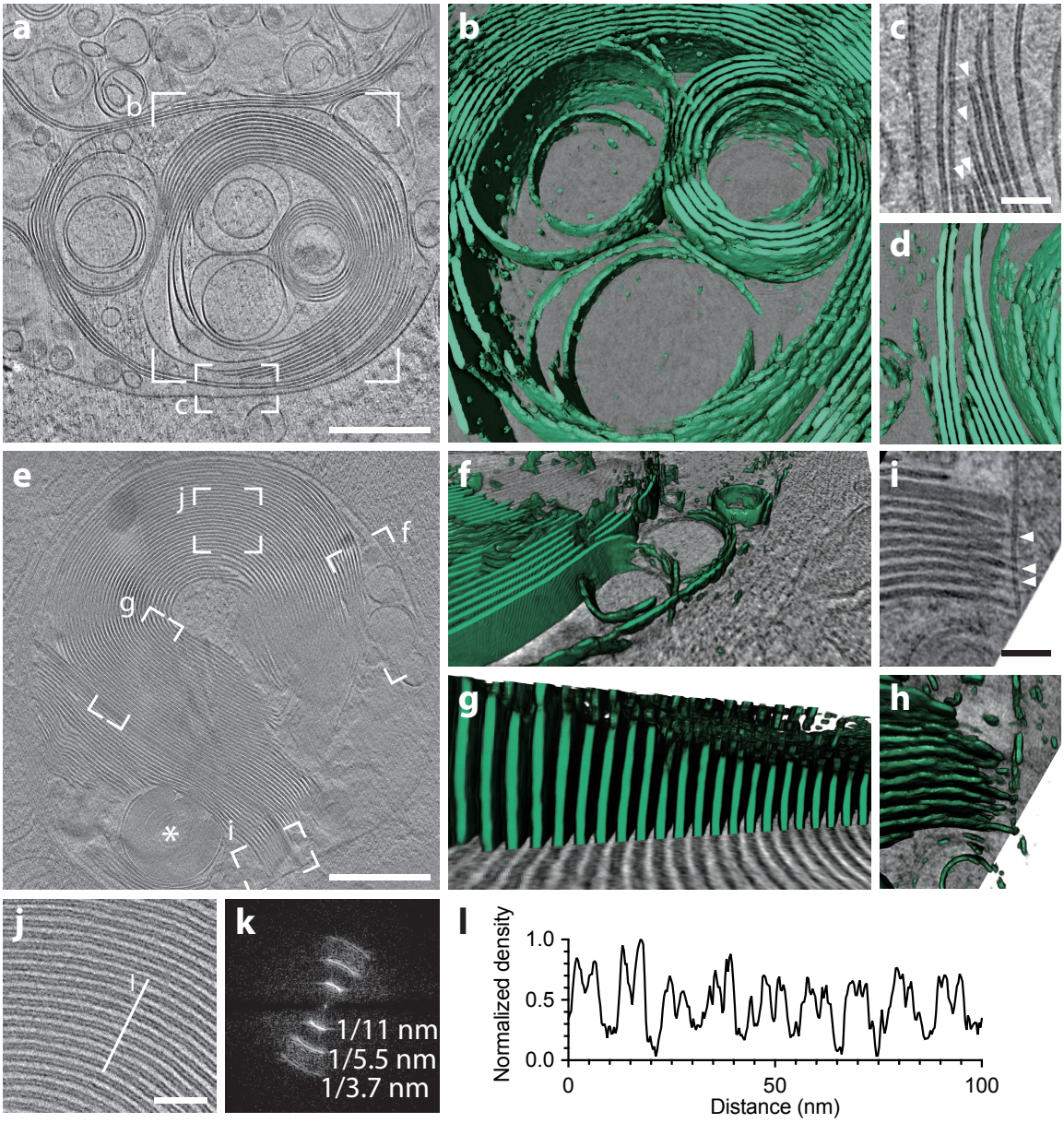

Fig. 4 | Cryo-ET of LB organelles reveals membrane packing and unique lipidic structures. a, Central slice of the reconstructed tomogram acquired at the site of the correlated ABCA3-eGFP signal. **b,** Rendering of the tomogram **(a)**. **c** and **d,** Detail of the tomogram showing membranes sheets with open ends (arrowheads) and rendering of the same region. **e,** Central slice through a tomogram of an ABCA3-eGFP positive organelle. A crystal-like structure is highlighted by an asterisk. **f,** 3D rendering of vesicles connecting to the limiting membrane and to the curved parallel membrane sheets. **g,** Rendering of the curved parallel membrane sheets. **i** and **h,** "T"-junctions (arrowheads) observed in the tomogram and in rendering. **j,** Parallel sheets observed in the lipidic core. **k,** FFT analysis of spacing in panel **(j)** reveals three major frequencies at 3.7 nm^{-1} (headgroup-headgroup), 5.5 nm^{-1} (bilayer width) and 11 nm^{-1}

(bilayer repeat). **l,** Plot of a line profile indicated by a white line in **(j)**. Scale bars: **(a, e)** 300 nm, **(c, i, j)** 50 nm

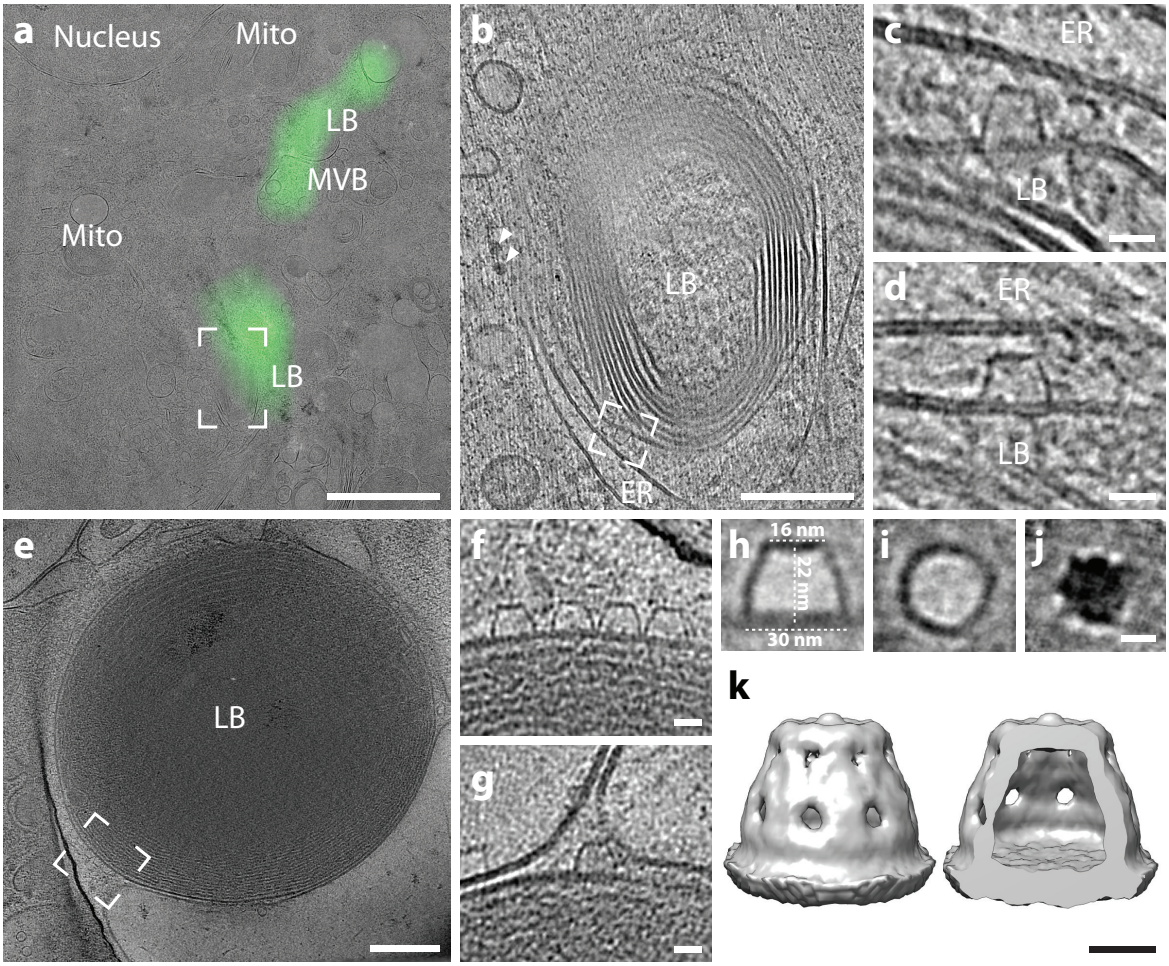

Fig. 5 |Outer membrane dome protein (OMDP) observed on the limiting membrane of LBs. a, Correlated image of a lamella with ABCA3-eGFP signal overlapping with a MVB and lamellar bodies. Nucleus and mitochondria (Mito) do not show the ABCA3-eGFP signal. **b,** Slice of a tomogram corresponding to the region indicated in **(a)** The ER cisterna is indicated. Ribosomes are marked with arrowheads. **c** and **d,** Two different slices of the same tomogram corresponding to the area indicated in **(b)**. OMDP assembly on a LB limiting membrane facing the membrane of a neighboring ER membrane. In total 3 identical assemblies are present in the tomogram shown in **(b)**. **e,** Slice of a tomogram showing a large LB at the cell periphery of long-term cultured A549 cells. Cells were directly used for whole-cell cryo-ET. **f,** Detail of a tomogram marked in **(e)** showing OMDPs. **g,** Detail of a tomogram corresponding to a marked region in **(e)** showing OMDP in proximity to a membrane of a neighboring organelle. **h-j,** Slices through a STA of 105 OMDPs found in 2 tomograms. **(h)** represents a XZ-slice through the center of the OMDP, **(i)** shows a XY-slice through the center and **(j)** through the top of the OMDP. **k,** Isosurface of the STA after applying C_8 symmetry. Scale bars: **(a)** 5 µm, **(b,e)** 200 nm, **(c, d, f, g)** 20 nm, **(h, i, j)** 10 nm, **(k)** 10 Å

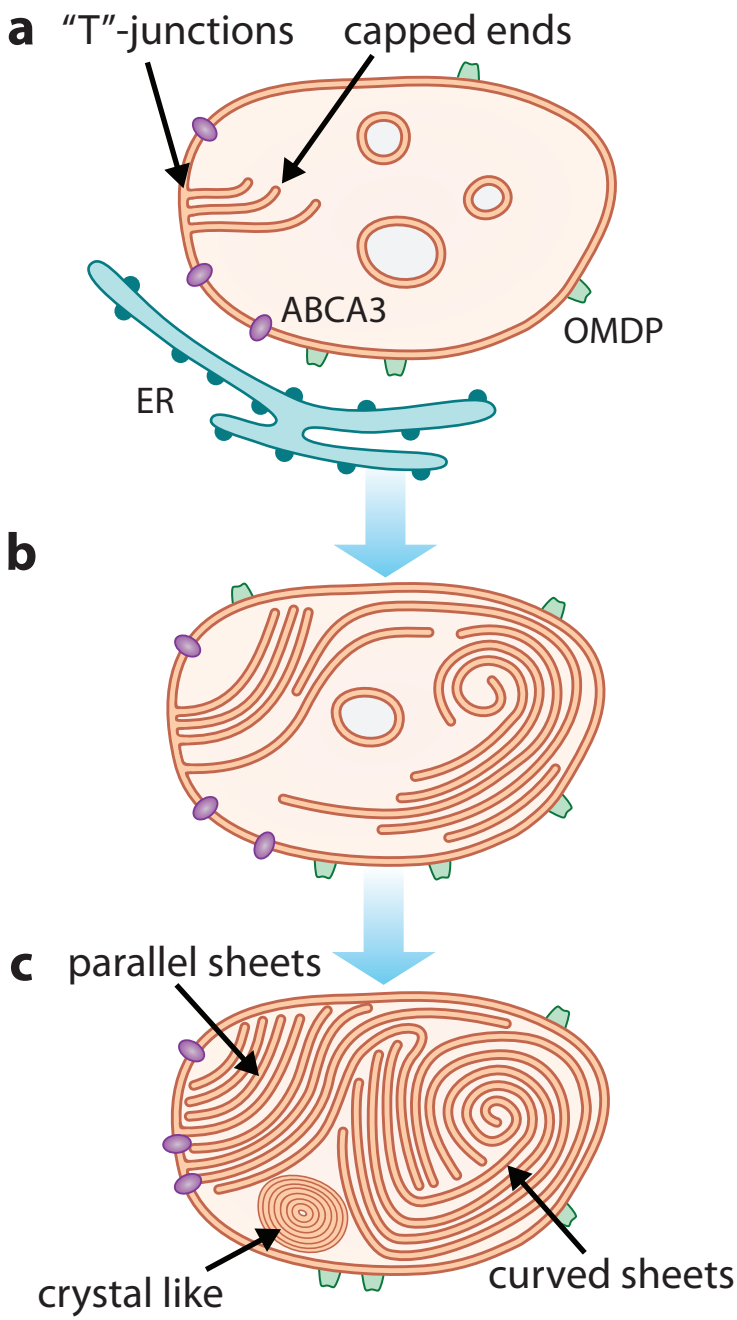

Fig. 6 | Proposed model of LB biogenesis. This model of LB biogenesis is based on observed ultrastructural features of LBs by cryo-TEM analysis. **a**, Early stage: phospholipids are transported to MVBs which are found in close proximity to ER cisternae. OMDPs found on the limiting membrane might play a role in this phospholipid transport. ABCA3 flips the phospholipids from the outer membrane leaflet to the inner one which results in a phospholipid asymmetry towards the inner leaflet. This leads to the formation of open-ended membrane protrusions which are directly connected to the limiting membrane by "T"-junctions. The open ends of these newly formed membrane sheets might be stabilized via capping by an unknown protein. **b**, Intermediate stage: membrane protrusions grow further and are eventually cleaved from the limiting membrane. Individual membrane sheets start to

organize in curved arrangements. **c**, Final stage: the lumen is packed with membrane sheets which form a combination of different structural arrangements including parallel straight and curved membranes as well as tightly packed crystal-like regions.

References

1. Daniels, C.B. & Orgeig, S. Pulmonary surfactant: the key to the evolution of air breathing. *News Physiol Sci* **18**, 151-157 (2003).
2. Ochs, M. The closer we look the more we see? Quantitative microscopic analysis of the pulmonary surfactant system. *Cell Physiol Biochem* **25**, 27-40 (2010).
3. Grathwohl, C., Newman, G.E., Phizackerley, P.J. & Town, M.H. Structural studies on lamellated osmiophilic bodies isolated from pig lung. 31P NMR results and water content. *Biochim Biophys Acta* **552**, 509-518 (1979).
4. Voorhout, W.F., Weaver, T.E., Haagsman, H.P., Geuze, H.J. & Van Golde, L.M. Biosynthetic routing of pulmonary surfactant proteins in alveolar type II cells. *Microsc Res Tech* **26**, 366-373 (1993).
5. Ridsdale, R., Na, C.L., Xu, Y., Greis, K.D. & Weaver, T. Comparative proteomic analysis of lung lamellar bodies and lysosome-related organelles. *PLoS One* **6**, e16482 (2011).
6. Hobi, N. *et al.* A small key unlocks a heavy door: The essential function of the small hydrophobic proteins SP-B and SP-C to trigger adsorption of pulmonary surfactant lamellar bodies. *Biochim Biophys Acta* **1863**, 2124-2134 (2016).
7. Mulugeta, S. *et al.* Identification of LBM180, a lamellar body limiting membrane protein of alveolar type II cells, as the ABC transporter protein ABCA3. *J Biol Chem* **277**, 22147-22155 (2002).
8. Matsumura, Y., Sakai, H., Sasaki, M., Ban, N. & Inagaki, N. ABCA3-mediated choline-phospholipids uptake into intracellular vesicles in A549 cells. *FEBS Lett* **581**, 3139-3144 (2007).
9. Perez-Gil, J. Structure of pulmonary surfactant membranes and films: the role of proteins and lipid-protein interactions. *Biochim Biophys Acta* **1778**, 1676-1695 (2008).
10. Vanhecke, D. *et al.* Lamellar body ultrastructure revisited: high-pressure freezing and cryo-electron microscopy of vitreous sections. *Histochem Cell Biol* **134**, 319-326 (2010).
11. Al-Amoudi, A., Studer, D. & Dubochet, J. Cutting artefacts and cutting process in vitreous sections for cryo-electron microscopy. *J Struct Biol* **150**, 109-121 (2005).
12. Rigort, A. *et al.* Focused ion beam micromachining of eukaryotic cells for cryoelectron tomography. *Proc Natl Acad Sci U S A* **109**, 4449-4454 (2012).
13. Marko, M., Hsieh, C., Schalek, R., Frank, J. & Mannella, C. Focused-ion-beam thinning of frozen-hydrated biological specimens for cryo-electron microscopy. *Nat Methods* **4**, 215-217 (2007).
14. Kukulski, W. *et al.* Correlated fluorescence and 3D electron microscopy with high sensitivity and spatial precision. *J Cell Biol* **192**, 111-119 (2011).
15. Schorb, M. & Briggs, J.A. Correlated cryo-fluorescence and cryo-electron microscopy with high spatial precision and improved sensitivity. *Ultramicroscopy* **143**, 24-32 (2014).

16. Metskas, L.A. & Briggs, J.A.G. Fluorescence-Based Detection of Membrane Fusion State on a Cryo-EM Grid using Correlated Cryo-Fluorescence and Cryo-Electron Microscopy. *Microsc Microanal* **25**, 942-949 (2019).
17. Sartori-Rupp, A. *et al.* Correlative cryo-electron microscopy reveals the structure of TNTs in neuronal cells. *Nat Commun* **10**, 342 (2019).
18. Plitzko, J.M., Rigort, A. & Leis, A. Correlative cryo-light microscopy and cryo-electron tomography: from cellular territories to molecular landscapes. *Curr Opin Biotechnol* **20**, 83-89 (2009).
19. Schellenberger, P. *et al.* High-precision correlative fluorescence and electron cryo microscopy using two independent alignment markers. *Ultramicroscopy* **143**, 41-51 (2014).
20. Hampton, C.M. *et al.* Correlated fluorescence microscopy and cryo-electron tomography of virus-infected or transfected mammalian cells. *Nat Protoc* **12**, 150-167 (2017).
21. Arnold, J. *et al.* Site-Specific Cryo-focused Ion Beam Sample Preparation Guided by 3D Correlative Microscopy. *Biophys J* **110**, 860-869 (2016).
22. Lieber, M., Smith, B., Szakal, A., Nelson-Rees, W. & Todaro, G. A continuous tumor-cell line from a human lung carcinoma with properties of type II alveolar epithelial cells. *Int J Cancer* **17**, 62-70 (1976).
23. Schmitz, G. & Muller, G. Structure and function of lamellar bodies, lipid-protein complexes involved in storage and secretion of cellular lipids. *J Lipid Res* **32**, 1539-1570 (1991).
24. Cooper, J.R. *et al.* Long Term Culture of the A549 Cancer Cell Line Promotes Multilamellar Body Formation and Differentiation towards an Alveolar Type II Pneumocyte Phenotype. *PLoS One* **11**, e0164438 (2016).
25. Castano-Diez, D., Kudryashev, M., Arheit, M. & Stahlberg, H. Dynamo: a flexible, user-friendly development tool for subtomogram averaging of cryo-EM data in high-performance computing environments. *J Struct Biol* **178**, 139-151 (2012).
26. Gorelick, S. *et al.* PIE-scope, integrated cryo-correlative light and FIB/SEM microscopy. *Elife* **8** (2019).
27. Faoro, R. *et al.* Aberration-corrected cryoimmersion light microscopy. *Proc Natl Acad Sci U S A* **115**, 1204-1209 (2018).
28. Wolff, G., Hagen, C., Grunewald, K. & Kaufmann, R. Towards correlative super-resolution fluorescence and electron cryo-microscopy. *Biol Cell* **108**, 245-258 (2016).
29. Haller, T., Cerrada, A., Pfaller, K., Braubach, P. & Felder, E. Polarized light microscopy reveals physiological and drug-induced changes in surfactant membrane assembly in alveolar type II pneumocytes. *Biochim Biophys Acta Biomembr* **1860**, 1152-1161 (2018).
30. Engelbrecht, S., Kaltenborn, E., Griese, M. & Kern, S. The surfactant lipid transporter ABCA3 is N-terminally cleaved inside LAMP3-positive vesicles. *FEBS Lett* **584**, 4306-4312 (2010).
31. Tanaka, H. *et al.* The structure of rat liver vault at 3.5 angstrom resolution. *Science* **323**, 384-388 (2009).
32. Weaver, T.E., Na, C.L. & Stahlman, M. Biogenesis of lamellar bodies, lysosome-related organelles involved in storage and secretion of pulmonary surfactant. *Semin Cell Dev Biol* **13**, 263-270 (2002).

33. Preibisch, S., Saalfeld, S. & Tomancak, P. Globally optimal stitching of tiled 3D microscopic image acquisitions. *Bioinformatics* **25**, 1463-1465 (2009).
34. Schindelin, J. *et al.* Fiji: an open-source platform for biological-image analysis. *Nat Methods* **9**, 676-682 (2012).
35. Wolff, G. *et al.* Mind the gap: micro-expansion joints drastically decrease the bending of FIB-milled cryo-lamellae. *bioRxiv*, 656447 (2019).
36. Mastronarde, D.N. Automated electron microscope tomography using robust prediction of specimen movements. *J Struct Biol* **152**, 36-51 (2005).
37. Hagen, W.J.H., Wan, W. & Briggs, J.A.G. Implementation of a cryo-electron tomography tilt-scheme optimized for high resolution subtomogram averaging. *J Struct Biol* **197**, 191-198 (2017).
38. Mastronarde, D.N. & Held, S.R. Automated tilt series alignment and tomographic reconstruction in IMOD. *J Struct Biol* **197**, 102-113 (2017).
39. Paul-Gilloteaux, P. *et al.* eC-CLEM: flexible multidimensional registration software for correlative microscopies. *Nat Methods* **14**, 102-103 (2017).